Inorganic Chemistry

Article

pubs.acs.org/IC

Oxoiron(IV) Complex of the Ethylene-Bridged Dialkylcyclam Ligand Me_2EBC

Jason England,[†,⊥] Jai Prakash,[†] Matthew A. Cranswick,[†,∥] Debasish Mandal,[§] Yisong Guo,*[,‡] Eckard Münck,*[,‡] Sason Shaik,*[,§] and Lawrence Que, Jr.*[,†]

[†]Department of Chemistry and Center for Metals in Biocatalysis, University of Minnesota, Minneapolis, Minnesota 55455, United States

[‡]Department of Chemistry, Carnegie Mellon University, Pittsburgh, Pennsylvania 15213, United States

[§]Institute of Chemistry and the Lise Meitner-Minerva Center for Computational Quantum Chemistry, The Hebrew University of Jerusalem, 91904 Jerusalem, Israel

Supporting Information

ABSTRACT: We report herein the first example of an oxoiron(IV) complex of an ethylene-bridged dialkylcyclam ligand, $[Fe^{IV}(O)(Me_2EBC)(NCMe)]^{2+}$ (**2**; Me_2EBC = 4,11-dimethyl-1,4,8,11-tetraazabicyclo[6.6.2]hexadecane). Complex **2** has been characterized by UV−vis, ^{1}H NMR, resonance Raman, Mössbauer, and X-ray absorption spectroscopy as well as electrospray ionization mass spectrometry, and its properties have been compared with those of the closely related $[Fe^{IV}(O)(TMC)(NCMe)]^{2+}$ (**3**; TMC = 1,4,8,11-tetramethyl-1,4,8,11-tetraazacyclotetradecane), the intensively studied prototypical oxoiron(IV) complex of the macrocyclic tetramethylcyclam ligand. Me_2EBC has an N4 donor set nearly identical with that of TMC but possesses an ethylene bridge in place of the 1- and 8-methyl groups of TMC. As a consequence, Me_2EBC is forced to deviate from the *trans*-I configuration typically found for $Fe^{IV}(O)(TMC)$ complexes and instead adopts a folded *cis*-V stereochemistry that requires the MeCN ligand to coordinate cis to the Fe^{IV}═O unit in **2** rather than in the trans arrangement found in **3**. However, switching from the trans geometry of **3** to the cis geometry of **2** did not significantly affect their ground-state electronic structures, although a decrease in ν(Fe═O) was observed for **2**. Remarkably, despite having comparable $Fe^{IV/III}$ reduction potentials, **2** was found to be significantly more reactive than **3** in both oxygen-atom-transfer (OAT) and hydrogen-atom-transfer (HAT) reactions. A careful analysis of density functional theory calculations on the HAT reactivity of **2** and **3** revealed the root cause to be the higher oxyl character of **2**, leading to a stronger O---H bond specifically in the quintet transition state.

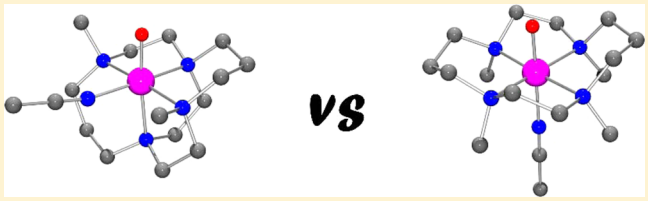

INTRODUCTION

Mononuclear nonheme iron enzymes are responsible for a remarkable number of biologically important transformations, including DNA and RNA repair, post-translational hydroxylation of amino acids, oxygen sensing, the biosynthesis of antibiotics, and histone demethylation in transcriptional regulation.[1,2] In the majority of cases, the active oxidant responsible for effecting these chemical transformations is an oxoiron(IV) species, which has been found to possess an S = 2 ground state in all examples spectroscopically characterized thus far.[3−8] Although it is not entirely clear whether these enzymatic intermediates possess an octahedral or a trigonal-bipyramidal geometry,[9,10] three of their ligands typically derive from the protein backbone, which leaves up to three coordination sites available for occupation by substrate, oxidant, or cofactor. Most importantly, these coordination sites are oriented cis with respect to one another and, by extension, the incipient Fe^{IV}═O moiety, a feature that is thought to be key to their function.

Since the turn of the century, a sizable family of synthetic oxoiron(IV) complexes has been reported.[11−13] More than 90% of these complexes exhibit an intermediate spin (S = 1) ground state rather than the S = 2 spin state established for the enzymatic intermediates. Much of our understanding of the spectroscopic and reactivity properties of these complexes has derived from the study of complexes containing solvent-occupied labile coordination sites, cis and/or trans to the Fe^{IV}═O moiety. The most extensively studied is the complex of 1,4,8,11-tetramethyl-1,4,8,11-tetraazacyclotetradecane (TMC; Chart 1), which coordinates in the equatorial plane with a *trans*-I stereochemistry,[14] resulting in a labile coordination site trans to the Fe^{IV}═O unit.[15] The array of complexes derived therefrom has been pivotal in building our current understanding of the reactivity properties of the oxoiron(IV) unit.[16−18] A further variation of the TMC ligand is the ethylene-bridged dialkylcyclam ligand 4,11-dimethyl-

Received: April 16, 2015
Published: August 5, 2015

DOI: 10.1021/acs.inorgchem.5b00861
Inorg. Chem. 2015, 54, 7828−7839

Chart 1

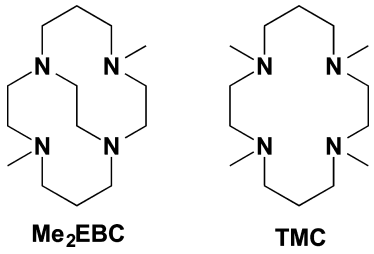

1,4,8,11-tetraazabicyclo[6.6.2]hexadecane (Me_2EBC; Chart 1), which is effectively identical with TMC in terms of the coordination environment but enforces a cis-coordination geometry.[14] Although the Me_2EBC ligand has been shown by Busch and co-workers to be able to stabilize the Mn^{IV} oxidation state[19,20] and an oxoiron(V) oxidant has been invoked in the catalytic epoxidation and cis-dihydroxylation of olefins with H_2O_2,[21] the corresponding iron(IV) chemistry has yet to be described. Herein, we report the synthesis, spectroscopic characterization, and reactivity of the oxoiron(IV) complex $[Fe^{IV}(O)(Me_2EBC)(NCMe)]^{2+}$ (**2**) and a comparison of its properties with those of $[Fe^{IV}(O)(TMC)(NCMe)]^{2+}$ (**3**).

EXPERIMENTAL SECTION

General Considerations. All reagents were purchased from commercial sources and used as received, unless otherwise noted. The complexes $[Fe^{II}(Me_2EBC)(Cl)_2]$ (**4**)[22] and $[Fe^{II}(Me_2EBC)(OTf)_2]$ (**5**)[21] and oxidant 2-(*tert*-butylsulfonyl)iodosylbenzene [2-(^{t}BuSO$_2$)C$_6$H$_4$IO][23] were synthesized according to previously published procedures. All moisture- and oxygen-sensitive compounds were prepared using standard Schlenk-line techniques, and a nitrogen-filled glovebox was used for any subsequent manipulation and storage of these compounds.

Preparation of Complexes. *$[Fe^{II}(Me_2EBC)(NCMe)_2](ClO_4)_2$ [**1**$(ClO_4)_2$].* A total of 2 equiv of $AgClO_4$ (0.24 g, 1.15 mmol) was added to a solution of **4** in MeCN (8 mL) and the resultant mixture stirred for 3 h. Subsequently, it was filtered to remove AgCl precipitate, which was itself washed with 3 mL of MeCN. The two batches of filtrate were combined and reduced in volume to approximately 3 mL. Diethyl ether (15 mL) was added, thereby causing precipitation of a solid, which was isolated by filtration, washed with diethyl ether, and dried under vacuum to give the product as a pale-green-brown powder (0.32 g, 94% yield). X-ray diffraction-quality crystals of **1**$(ClO_4)_2$ were obtained by vapor diffusion of Et_2O into a concentrated MeCN solution of the complex. ^{1}H NMR (CD_3CN, 293 K, all peaks appear as broad singlets): δ 283 (2H, CH_2), 246 (2H, CH_2), 128 (2H, CH_2), 107 (2H, CH_2), 84 (2H, CH_2), 72 (6H, N*Me*), 60 (2H, CH_2), 40 (2H, CH_2), 23 (2H, CH_2), 11 (2H, CH_2), −8.1 (2H, CH_2), −55 (2H, CH_2). MS (ESI$^+$): m/z 409.2 ($[Fe^{II}(Me_2EBC)(ClO_4)]^+$). Anal. Calcd (found) for $C_{18}H_{36}Cl_2FeN_6O_8$: C, 36.55 (36.29); H, 6.14 (6.30); N, 14.22 (13.79).

*$[Fe^{II}(Me_2EBC)(OTf)_2]$ (**5**).* Compound **5** was synthesized following an earlier published literature procedure.[21] ^{1}H NMR (CD_2Cl_2, 293 K, all peaks appear as broad singlets): δ 309.7 (2H, CH_2), 246.5 (2H, CH_2), 126.1 (2H, CH_2), 88.6 (6H, N*Me*), 88.2 (2H, CH_2), 77.6 (2H, CH_2), 72.1 (2H, CH_2), 63.7 (2H, CH_2), 23.3 (2H, CH_2), 18.4 (2H, CH_2), 1.7 (2H, CH_2), −6.1 (2H, CH_2), −109.2 (2H, CH_2). MS (ESI$^+$): m/z 459.3 ($[Fe^{II}(Me_2EBC)(OTf)]^+$).

*$[Fe^{IV}(O)(Me_2EBC)(NCMe)]^{2+}$ (**2**).* To a stirring MeCN solution of **5** at 0 °C was added 1.5 equiv of 2-(^{t}BuSO$_2$)C$_6$H$_4$IO dissolved in CH_2Cl_2. The progress of the reaction was monitored spectrophotometrically and, after 3−5 min, resulted in the maximal formation of **2**. ^{1}H NMR (CD_3CN, 293 K, all peaks appear as broad singlets): δ 38 (1H, CH_2), 29 (1H, CH_2), 21 (1H, CH_2), 20 (1H, CH_2), 15 (1H, CH_2), 9.4 (1H, CH_2), 4.6 (1H, CH_2), 4.1 (1H, CH_2), −5.5 (2H, CH_2), −9.4 (1H, CH_2), −9.8 (1H, CH_2), −12 (1H, CH_2), −19 (1H, CH_2), −29 (1H, CH_2), −31 (3H, N*Me*), −45 (3H, N*Me*), −67 (1H, CH_2), −81 (1H, CH_2), −83 (1H, CH_2), −107 (1H, CH_2), −124 (1H, CH_2), −169 (1H, CH_2), −211 (1H, CH_2). MS (ESI$^+$): m/z 475.4 ($[Fe^{IV}(O)(Me_2EBC)(OTf)]^+$), 163.2 ($[Fe^{IV}(O)(Me_2EBC)]^{2+}$).

Physical Methods. NMR spectra were recorded in deuterated solvents using either Varian Inova 500 or 300 MHz spectrometers, and chemical shifts (ppm) were referenced to residual protic solvent peaks. Elemental analyses were carried out by Atlantic Microlab (Norcross, GA). UV−vis spectroscopic measurements were performed using a HP8453A diode-array spectrometer equipped with a cryostat from Unisoku Scientific Instruments (Osaka, Japan). Electrospray ionization mass spectrometry (ESI-MS) experiments were carried out on a Bruker BioTOF II mass spectrometer using a spray chamber voltage of 4000 V and a carrier gas temperature tailored according to the stability of the complex (200 and 70 °C for complexes **1** and **2**, respectively). Mössbauer spectra were recorded with home-built spectrometers using Janis Research Super-Varitemp dewars, which allowed studies in the temperature range of 1.5−200 K and applied magnetic fields of up to 8.0 T. Mössbauer spectral simulations were performed using the *WMOSS* software package (SEE Co., Edina, MN), and isomer shifts (δ) are quoted relative to iron metal at 298 K.

X-ray Crystallography. A selected single crystal of **1**$(ClO_4)_2$ was placed on the top of a 0.1-mm-diameter glass capillary and mounted on a Bruker SMART V5.054 CCD area detector diffractometer for data collection at 123(2) K. A preliminary set of cell constants was collected from reflections harvested from three sets of 20 frames. These initial sets of frames were oriented such that orthogonal wedges of reciprocal space were surveyed. Using 54 reflections (14 were not indexed), initial orientation matrixes were produced. These reflections were indexed as a two-component twin related by a 180° rotation about the *a* axis (see the CIF file for additional details) using *CELL_NOW*.[24] Data collection was carried out using Mo Kα radiation (graphite monochromator) with a frame time of 60 s and a detector distance of 4.8 cm. A randomly oriented region of the reciprocal space was surveyed to the extent of one sphere and to a resolution of 0.84 Å, with four major sections of frames being collected using 0.30° steps in ω at four different ϕ settings and a detector position of −28° in 2θ. The intensity data were corrected for absorption and decay (*TWINABS*).[25] Final cell constants were calculated from 2947 strong reflections taken from the actual data collection after integration (*SAINT*).[26] Please refer to Table S1 for a summary of the crystallographic and structure refinement data.

The structures were solved and refined using Bruker *SHELXTL*.[27] The space group $P2_1/c$ was determined based on systematic absences and intensity statistics. A direct methods solution was calculated that provided most non-hydrogen atoms from the *E*-map. The remaining non-hydrogen atoms were located by full-matrix least-squares/difference Fourier cycles. All non-hydrogen atoms were refined with anisotropic displacement parameters. All hydrogen atoms were placed in ideal positions and refined as riding atoms with relative isotropic displacement parameters. The pattern of difference Fourier peaks suggests a minor occupancy of the enantiomorph at 5−10%.

Crystallographic data for **1**$(ClO_4)_2$ have been deposited with the Cambridge Crystallographic Data Centre with a deposition number of CCDC 1029038.

Resonance Raman Spectroscopy. Resonance Raman spectra of **2** were collected in a frozen solution at 77 K using a Spectra-Physics model 2060 Kr^+ laser and an ACTON AM-506 monochromator equipped with a Princeton LN/CCD data collection system. Samples in a 20:1 CH_3CN/CH_2Cl_2 or a 20:1 CD_3CN/CD_2Cl_2 solution were frozen onto a gold-plated copper coldfinger in thermal contact with a Dewar flask containing liquid nitrogen. Throughout, the monochromator slit width was set for a band pass of 4 cm^{-1}, and a 135° backscattering geometry was used. Spectra were collected using λ_{ex} = 406.7 nm at 20 mW, and plotted spectra were composed from an average of 32 scans with collection times of 30 s. Raman frequencies were calibrated to indene prior to data collection. All spectra were intensity-corrected to the 710 or 773 cm^{-1} solvent peak of CD_3CN or CH_3CN, respectively.

DOI: 10.1021/acs.inorgchem.5b00861
Inorg. Chem. 2015, 54, 7828−7839

X-ray Absorption Spectroscopy (XAS). XAS data were collected on beamline 7-3 of the Stanford Synchrotron Radiation Lightsource (SSRL) of the SLAC National Accelerator Laboratory. Fe K-edge XAS data were collected for frozen samples of **2** prepared in tandem XAS/Mössbauer cups with $[Fe]_{total} \sim 4-5$ mM. The SPEAR storage ring of the SSRL was operated at 3.0 GeV and ~350 mA, and energy resolution of the focused incoming X-rays was achieved using a Si(220) double-crystal monochromator, which was detuned to 50% of maximal flux to attenuate second-harmonic X-rays. The sample temperature was controlled utilizing an Oxford Instruments CF1208 continuous-flow liquid-helium cryostat. Data were obtained as fluorescence excitation spectra with a 31-element solid-state germanium detector array (Canberra). An iron foil spectrum was recorded concomitantly for internal energy calibration, and the first inflection point of the K-edge was assigned to 7112.0 eV. The edge energy was monitored during data collection for red shifts indicative of sample photoreduction, but none were observed in the present study. A 3 μm manganese foil and a Soller slit were utilized to attenuate the signal-to-noise of the incoming data counts. The data set obtained by averaging 15 scans was used in spectral analysis.

Data reduction, averaging, and normalization were performed using the program *EXAFSPAK*.[28] Following calibration and averaging of the data, background absorption was removed by fitting a Gaussian function to the preedge region and then subtracting this function from the entire spectrum. A three-segment spline with fourth-order components was then fit to the extended X-ray absorption fine structure (EXAFS) region of the spectrum in order to extract $\chi(k)$.

Theoretical phase and amplitude parameters for a given absorber–scatterer pair were calculated using *FEFF 8.40*[29] and utilized by the "opt" program of the *EXAFSPAK* package during curve fitting.[28] Parameters for **2** were calculated using the crystal structure coordinates of **1**, modified to possess bond distances and ligands similar to those of the crystallographically determined structure of **3**. In all analyses, the coordination number of a given shell was a fixed parameter and was varied iteratively, while bond lengths (r) and mean-square deviations (σ^2) were allowed to freely float. The amplitude reduction factor S_0 was fixed at 0.9, while the edge shift parameter E_0 was allowed to float as a single value for all shells [thus, in any given fit, the number of floating parameters was typically equal to (2 × number of shells) + 1]. The goodness-of-fit F was defined simply as $\sum(\chi_{exptl} - \chi_{calc})$.[2] For fits to unfiltered data, a second goodness-of-fit parameter, F-factor, was defined as $[\sum k^6(\chi_{exptl} - \chi_{calc})^2/\sum k^6\chi_{exptl}^2]^{1/2}$. In order to account for the effect that additional shells have on improving the fit quality, a third goodness-of-fit metric $F' = F^2/(N_{IDP} - N_{VAR})$ was employed, where N_{VAR} is the number of floated variables in the fit and N_{IDP} is the number of independent data points, which is defined as $N_{IDP} = 2\Delta k\Delta r/\pi$. In the latter equation, Δk is the k range over which the data are fit, while Δr is the back-transformation range employed in fitting Fourier-filtered data. F' is thus of principal utility in fitting Fourier-filtered data but can also be employed for unfiltered data by assuming a large value of Δr.

Preedge analysis was carried out by normalization of the data in the *Ifeffit* program *Athena*,[30] and fitting the restricted preedge region (7105–7120 eV), as suggested by Westre et al.,[31] using the program *Fityk*.[32] The preedge transition was fit using a Gaussian function, and a pseudo-Voigt baseline function composed of 50:50 Gaussian/Lorentzian functions.

Density Functional Theory (DFT) Calculations. *Structural and Spectroscopic Studies.* DFT calculations were performed using Becke's three-parameter hybrid (B3LYP) functional and basis set 6-311G provided by *Gaussian09* software package.[33] The initial structural model for **2** was constructed using the crystal structure of **1** by replacing one of the CH_3CN ligands with an oxygen atom. The self-consistent-field procedure and geometry optimization were terminated upon reaching the default convergence criteria. The quadrupole splitting ΔE_Q was calculated using the property keyword of the Gaussian code and $Q(^{57}Fe) = 0.17$ barn. The ^{57}Fe isomer shift δ was evaluated from the DFT charge density at the iron nucleus using the calibration given by Vrajmasu et al.[34]

Reactivity Studies. All of the computational details are given in the Supporting Information. A few details follow here. The hydrogen-atom-transfer (HAT) process for **2** and **3** reacting with 9,10-dihydroanthracene (DHA) was studied by means of DFT calculations. Geometry optimization was conducted with UB3LYP. For all of the species, we used the LACVP*(Fe)/6-31G*(rest) basis set, labeled B1. To avoid the self-interaction errors, we neutralized the charge of the oxoiron(IV) reagents with ClO_4^- for **2** and triflate ($CF_3SO_3^-$) counterions for **3** and verified that there are no consequences to the usage of different counterions. Geometry optimization at the B1 level of theory was carried out with the *Jaguar 8.0* program.[35] A subsequent frequency calculation were also done at the same level to confirm the nature of the optimized structures as local minima (no imaginary frequency) or transition states (one imaginary frequency) and to evaluate the zero-point vibrational energy and thermal corrections to the Gibbs free energy at T = 273 K, which is the experimental temperature.

The energies were further corrected with two larger basis sets, LACV3P+*(Fe)/6-311+G*, labeled B2, and the all-electron Def2-TZVPP basis set, labeled B3. Solvent effect corrections on B1 geometries were carried out at the B2 and B3 levels, at the latter using the PCM model with the default UFF radii in *Gaussian09*. Tunneling and kinetic isotope (KIE) effects were calculated to validate the mechanism.[36]

Reaction Kinetics. All kinetic studies were performed under a nitrogen atmosphere. MeCN solutions of **2** (0.5 mM) were prepared by treating **1** with 1.5 equiv of 2-(^{t}BuSO$_2$)C$_6$H$_4$IO dissolved in CH_2Cl_2 or trifluoroethanol at 0 °C. Organic substrates dissolved in either CH_2Cl_2 [PPh_3, DHA, 1,4-cyclohexadiene (CHD)] or MeCN (thioanisole and benzyl alcohol) were added in >10-fold excess to the aforementioned solutions of **2** at either −40 or 0 °C. The resulting reactions were monitored by decay of the near-IR feature (λ_{max} = 800 nm) associated with the oxoiron(IV) complex and found to display *pseudo*-first-order kinetics. Plots of the observed rate constants (k_{obs}) versus substrate concentration were found to be linear in all cases (Figures S1–S6), thereby yielding second-order rate constants (k_2).

RESULTS AND DISCUSSION

Synthesis and Characterization of [Fe^{II}(Me$_2$EBC)(NCMe)$_2$](X)$_2$ [1(X)$_2$; X = OTf, ClO$_4$]. Although the iron(II) starting complex **5** could be generated by the combination of equimolar quantities of Me$_2$EBC and [Fe^{II}(OTf)$_2$(NCMe)$_2$] in CH_2Cl_2 solution, it was more reliably and cleanly prepared by metathesis of the chloride ligands in **4** using AgOTf. It was previously demonstrated, using ^{19}F NMR spectroscopy, that in MeCN solution **5** actually exists as the solvento complex **1**(OTf)$_2$.[21] Hence, efforts were made to grow crystals of the latter suitable for X-ray crystallographic analysis. This was unsuccessful, so other salts of **1** were prepared in MeCN solution via silver salt metathesis, and the resulting materials were recrystallized.

It was found that recrystallization of **1**(ClO$_4$)$_2$ yielded pale-green-brown crystals suitable for X-ray analysis, and the structure of the [Fe^{II}(Me$_2$EBC)(NCMe)$_2$]$^{2+}$ ion (**1**) is presented in Figure 1. As anticipated, the dication is six-coordinate and *pseudo*-C_2-symmetric, and the Me$_2$EBC ligand adopts the *cis*-V stereochemistry typically seen in its complexes, with the two MeCN ligands occupying cis-coordination sites.[14,19–22] This is in sharp contrast to the five-coordinate *trans*-I geometry displayed in all X-ray structures of nonbridged tetralkylcyclam iron(II) complexes reported thus far,[14,18,37,38] in which a nominally vacant site is trans to the axial noncyclam ligand and all four *N*-alkyl substituents are oriented syn with respect to one another. Interestingly, the average Fe–N$_{3°\text{-amine}}$ bond length in **1** is 2.06 Å, considerably shorter than those found in high-spin Fe^{II}(Me$_2$EBC) complexes **4** (2.27 Å) and **5**

DOI: 10.1021/acs.inorgchem.5b00861
Inorg. Chem. 2015, 54, 7828–7839

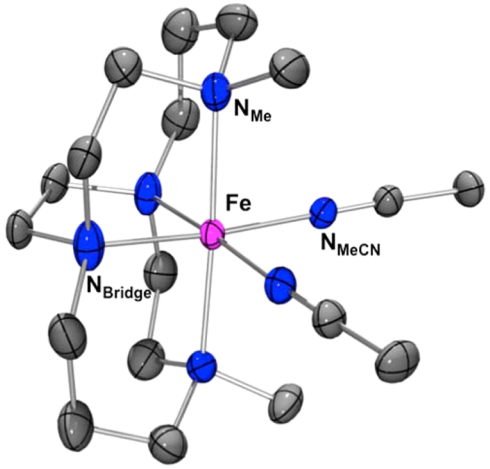

Figure 1. Structure of the dicationic component of $\mathbf{1}(ClO_4)_2$, depicted using 50% probability ellipsoids. Hydrogen atoms and ClO_4^- counterions have been omitted for clarity. Atom color scheme: C, gray; N, blue; Fe, magenta.

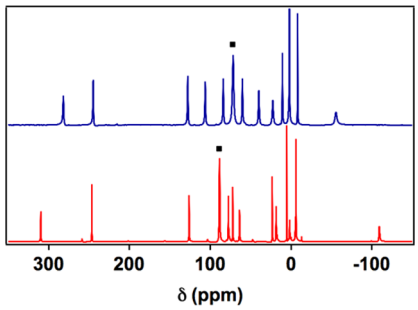

Figure 2. ^{1}H NMR spectra of **5** recorded in CD_3CN (top) and CD_2Cl_2 (bottom) at room temperature. The N*Me* resonances are marked with "■".

(2.20 Å) but comparable to those in low-spin $Fe^{II}(R_3TACN)$ complexes (Table 1).[21,22] In addition, the Fe−N_{MeCN} bond lengths of **1** (1.94 Å) compare well to those found in the low-spin complexes $[Fe^{II}(TPA)(NCMe)_2]^{2+}$ (1.93 Å) and $[Fe^{II}(Me_3TACN)(NCMe)_3]^{2+}$ (1.98 Å) but are about 0.2 Å shorter than those seen in the high-spin complexes $[Fe^{II}(Me_3TACN)(NCMe)_2(OTf)]^+$ (2.14 Å) and $[Fe^{II}(6\text{-}Me_3TPA)(NCMe)_2]^{2+}$ (2.17 Å).[39,40] These bond-length differences reflect the decrease in the ionic radius upon a change in the spin state and are thus diagnostic of the spin state of the iron(II) center. Thus, the iron(II) center in **1** is likely to be low-spin, a property that is confirmed by Mössbauer studies (Figure S7). As such, $\mathbf{1}(ClO_4)_2$ represents the first instance of a low-spin iron(II) tetraalkylcyclam complex.

On the basis of the crystal structure of $\mathbf{1}(ClO_4)_2$, one might expect the peaks in its ^{1}H NMR spectrum in a CD_3CN solution to be restricted to the diamagnetic region (0−10 ppm), but this is not the case. In fact, its room temperature ^{1}H NMR spectrum shows strongly paramagnetically shifted resonances spread out over the chemical shift range of +280 to −60 ppm (Figure 2, top), suggesting that **1** is a high-spin iron(II) complex in solution at 25 °C. More specifically, the ^{1}H NMR spectrum of **1** contains 11 peaks that integrate to two protons each, plus one peak that integrates to six protons, which can be assigned to the methyl substituents. This is consistent with **1** possessing C_2 symmetry in solution, but in such a scenario, one would expect the spectrum to contain 12 peaks that integrate to two protons each. Hence, one peak (two protons) is missing, presumably due to either severe line broadening resulting from very close proximity to the metal center, which can lead to inaccurate peak integration and even complete loss of a signal, or overlap with the intense solvent signals in the diamagnetic region.

Interestingly, contrary to expectations based upon Curie's law by which the chemical shifts would be expected to increase linearly with $1/T$, the chemical shift range decreased to +190 to −50 ppm at −40 °C (Figure S8). These results suggest the existence of a rapid equilibrium between high- and low-spin forms of **1**, i.e., spin-crossover behavior, which has been noted for a wide array of $Fe^{II}(N6)$ complexes.[45,46] Similar behavior was also reported for the related $[Fe^{II}(BPMEN)(NCMe)_2](ClO_4)_2$ [BPMEN = *N*,*N*′-dimethyl-*N*,*N*′-bis(2-pyridylmethyl)-1,2-diaminoethane] and $[Fe^{II}(BQMEN)(NCMe)_2](ClO_4)_2$ [BQMEN = *N*,*N*′-dimethyl-*N*,*N*′-bis(8-quinolylmethyl)-1,2-diaminoethane] complexes.[47−49] The ^{1}H NMR spectrum of **5** obtained in CD_2Cl_2 at 25 °C exhibits an even larger spread of chemical shifts (Figure 2, bottom) that presumably arises only from the high-spin complex. Titration of this solution with CD_3CN resulted first in the appearance of a spectrum with twice the number of signals, consistent with the loss of 2-fold symmetry, and upon addition of more CD_3CN, a spectrum like that of **1** in pure CD_3CN was obtained (Figure S9). These changes reflect the stepwise replacement of the triflate ligands of **5** with CD_3CN via the C_1-symmetric monotriflate complex, which was also corroborated by ^{19}F NMR (Figure S10). They

Table 1. Bond Lengths (Å) of $[Fe^{II}(Me_2EBC)(X)_2]$ and Related Complexes[a]

complex	*S*	Fe−N_{Me}	Fe−N_{bridge}	Fe−X	ref
$[Fe^{II}(Me_2EBC)(NCMe)_2](ClO_4)_2$ [$\mathbf{1}(ClO)_4$]	0	2.073(4), 2.094(4)	2.027(4), 2.037(4)	1.942(4), 1.946(4)	this work
$[Fe^{II}(Me_2EBC)Cl_2]$ (**4**)	2	2.2748(13), 2.2866(14)	2.2574(13), 2.2634(13)	2.4260(5), 2.4273(4)	22
$[Fe^{II}(Me_2EBC)(OTf)_2]$ (**5**)	2	2.1992(13), 2.1993(13)	2.1973(13), 2.1974(13)	2.1243(11), 2.1244(11)	21
$[Fe^{II}(TMC)(NCS)](OTf)$	2	2.20		2.018(4)	41
$[Fe^{II}(TMC)(O_2SPh)](OTf)$	2	2.22		1.996(2)	37
$[Fe^{II}(^{Me,H}PyTACN)(NCMe)_2](PF_6)_2$	0	2.00			42
$[Fe^{II}(^{Me,H}PyTACN)(OTf)_2]$	2	2.21			43
$[Fe^{II}(^{Me,6Me}PyTACN)(NCMe)_2](SbF_6)_2$	0	2.03			44
$[Fe^{II}(^{Me,6Me}PyTACN)(OTf)_2]$	2	2.23			43
$[Fe^{II}(Me_3TACN)(NCMe)_3](BPh_4)_2$	0	2.05		1.98	40
$[Fe^{II}(Me_3TACN)(NCMe)_2(OTf)](OTf)$	2	2.20		2.14	40

[a]Abbreviations used: ^{Me,H}PyTACN = 1-(pyridyl-2′-methyl)-4,7-dimethyl-1,4,7-triazacyclononane; ^{Me,6Me}PyTACN = 1-(6′-methylpyridyl-2′-methyl)-4,7-dimethyl-1,4,7-triazacyclononane; Me_3TACN = 1,4,7-trimethyl-1,4,7-triazacyclononane.

DOI: 10.1021/acs.inorgchem.5b00861
Inorg. Chem. 2015, 54, 7828−7839

also show that the triflate and MeCN ligands in the monotriflate complex are in slow exchange with respect to the possible positional isomers.

Preparation and Characterization of 2. The reaction of **1** with 1.5 equiv of 2-(^{t}BuSO$_2$)C$_6$H$_4$IO at 0 °C results in the rapid formation of yellow species **2**, possessing a half-life ($t_{1/2}$) of 5 h and characterized by an intense UV band at 282 nm (ε_{max} ~ 13000 M^{-1} cm^{-1}) and weak near-IR features centered at 800 (ε_{max} ~ 270 M^{-1} cm^{-1}) and 945 nm (Figure 3 and Table 2).

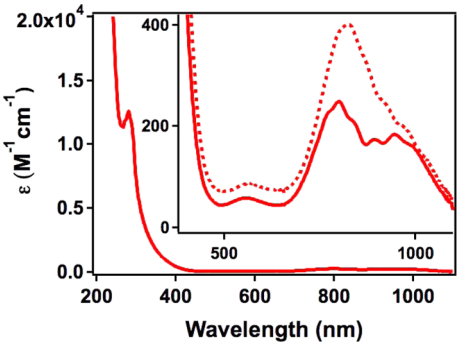

Figure 3. Electronic spectra of **2** (solid) and **3** (dashed) recorded in a MeCN solution at 0 °C.

Table 2. Spectroscopic Properties of Oxoiron(IV) Tetraalkyltetraazamacrocyclic Complexes

	2[a]	3[b]
λ_{max} (nm) [ε_{max} (M^{-1} cm^{-1})]	282, 540, 800, 945 [13000, 80, 270, 190]	282, 824 [10000, 400]
ν(Fe=O) (cm^{-1}) [Δ^{18}O]	824 [−45]	839 [−35]
	Mössbauer Analysis	
δ (mm s^{-1})	0.13(1) (0.15)	0.17
ΔE_Q (mm s^{-1})	0.60(2) (*0.34*)	1.24
η	0.4 (0.9)	0.5
D (cm^{-1})	26(2)	26.95[c]
$A_{x,y,z}/g_n\beta_n(T)$	−22(1), −21(1), −3(2) (*−21, −20, −5*)	−21.3, −20.3, −2.9[d]
	XAS Analysis	
E_0 (eV)	7124.5	7124.5
$E_{preedge}$ (eV)	7114.0	7114.1
preedge area[e]	33	33
r(Fe=O) (Å)	1.64 (1.65)	1.64
r(Fe−N)$_{ave}$ (Å)	2.04 (*2.08*)	2.08

[a]Italicized numbers within parentheses represent values obtained from DFT calculations. The calculated **A** tensor was obtained by taking the experimentally determined A_{iso} and adding the spin-dipolar term obtained from DFT. [b]Data from ref 52. [c]Reference 53. [d]Reference 54. [e]Weighted preedge areas scaled to values expected for the pure oxoiron(IV) complex, assuming that other impurities present do not contribute significantly to the preedge area.

[Titration of 2-(^{t}BuSO$_2$)C$_6$H$_4$IO into solutions of **1** provided maximal yields of **2** when 1.5 equiv of the oxidant was used.] The latter is emblematic of S = 1 oxoiron(IV) complex formation and is attributed to symmetry-forbidden ligand-field (d → d) transitions.[50,51] A further noteworthy point is that the near-IR feature of **2** shows rich vibronic structure, which was also seen for **3**[15] but is not apparent in the UV−vis spectra of the majority of S = 1 oxoiron(IV) complexes. The successful formation of an oxoiron(IV) complex is further evidenced by the ESI-MS spectrum of **2**. In addition to the features associated with **1**, it exhibits two prominent ion fragments (Figures S11 and S12), with m/z 475 and 163 possessing isotope distribution patterns consistent with respective formulations as [Fe^{IV}(O)(Me$_2$EBC)(OTf)]$^+$ and [Fe^{IV}(O)-(Me$_2$EBC)]$^{2+}$.

The ^{1}H NMR spectrum of **2** exhibits a set of 24 paramagnetically shifted resonances in the chemical shift range of +40 to −210 ppm (Figure 4) and is free of starting

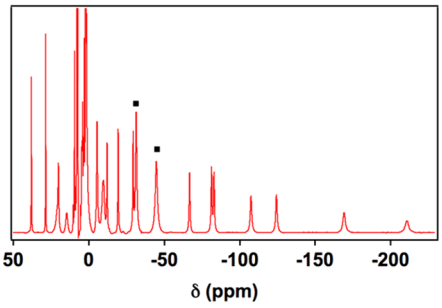

Figure 4. ^{1}H NMR spectrum of **2** recorded in CD$_3$CN at room temperature. The N*Me* resonances are marked with "■".

material **1** (Figure 2). Many upfield-shifted resonances are observed, which is typical of S = 1 iron(IV) centers, while the reverse is normally found for S = 2 iron(II) complexes.[18,54,55] Of the 24 peaks, there are two peaks that integrate to three protons each, corresponding to the two methyl groups and 22 signals with one-proton integration assigned to the diastereotopic methylene protons. (As was the case in **1**, two protons are missing from the spectrum of **2**.) Complex **2** has twice the number of peaks as that seen for **1**, which is indicative of formation of the C_1-symmetric complex **2**, where a MeCN ligand is coordinated cis to the oxo-atom donor and in the slow-exchange regime relative to the two possible positional isomers.

Resonance Raman spectroscopy of a 10 mM solution of **2** in 20:1 MeCN/CH$_2$Cl$_2$ using λ_{ex} = 406.7 nm yields a resonance-enhanced band at 824 cm^{-1}, which is in the energy range typically associated with ν(Fe=O) of oxoiron(IV) complexes (Figure 5). Generation of **2** using an ^{18}O-labeled oxidant leads to loss of the 824 cm^{-1} feature and the appearance of two new resonance-enhanced bands at 766 and 791 cm^{-1}. Assuming that

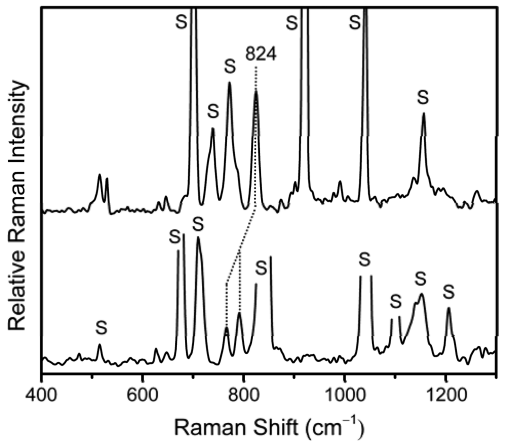

Figure 5. Resonance Raman spectrum of **2** in 20:1 MeCN/CH$_2$Cl$_2$ (top) and its ^{18}O-labeled isotopomer in 20:1 CD$_3$CN/CD$_2$Cl$_2$ (bottom). λ_{ex} = 406.7 nm; power = 20 mW; [Fe] = 10 mM.

DOI: 10.1021/acs.inorgchem.5b00861
Inorg. Chem. 2015, 54, 7828−7839

the 766 and 791 cm^{-1} bands are due to a ν(Fe=O) Fermi doublet (ν^0 = 779 cm^{-1}), this corresponds to a 45 cm^{-1} shift upon ^{18}O labeling (equal weighting was given to the two peaks), which is significantly larger than that predicted by Hooke's law for a diatomic harmonic oscillator (−37 cm^{-1}). For most nonheme Fe^{IV}=O complexes thus far characterized by resonance Raman spectroscopy, the ^{18}O shifts observed are either as-predicted for a diatomic vibration by Hooke's law or slightly lower.[11] There are, however, the three following exceptions: ν(Fe=O) for [(6-Me_3TPA)Fe^{III}OFe^{IV}(O)(6-Me_3TPA)]$^{3+}$ observed at 840 cm^{-1} with a 43 cm^{-1} downshift upon ^{18}O labeling of the oxo group,[56] that for [(*cis*-β-BPMCN)Fe^{IV}(O)]$^{2+}$ at 822 cm^{-1} with a 40 cm^{-1} downshift,[57] and that for [(^{Me,H}PyTACN)Fe^{IV}(O)]$^{2+}$ at 831 cm^{-1} with a 43 cm^{-1} downshift.[58] Although the reasons for such discrepancies are presently unclear, the assignment of these vibrations as ν(Fe=O) is not in doubt. ν(Fe=O) of **2** is approximately 15 cm^{-1} lower in energy than that of **3**, which implies that the Fe=O bond in the former is weaker than that in the latter. On the basis of previously established trends,[52,59] this might be expected to translate into **2** displaying greater reactivity than **3**.

The 4.2 K zero-field Mössbauer spectrum of a frozen solution of **2** contains a quadrupole doublet representing 75% of the total iron, with ΔE_Q = 0.60 mm s^{-1} and δ = 0.13 mm s^{-1} (Figure 6, top). This δ value is close to that obtained for **3** (Table 2)[15] and typical of S = 1 oxoiron(IV) complexes.[11] The magnetic hyperfine interactions and parameters obtained from the applied field measurements shown in Figure 6 confirm this assumption. Interestingly, the ΔE_Q value obtained for **2** is approximately half the size of that for **3**, which may reflect a decrease in the axial symmetry accompanying the fact that the MeCN ligand is cis, and not trans, to the oxo ligand.

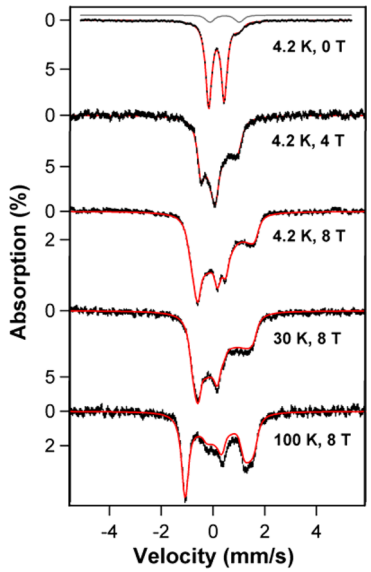

Figure 6. Mössbauer spectra of **2** recorded at the various temperatures and parallel applied fields indicated. The sample contained 20% high-spin ferric impurity, and its 4.2 K spectral features were simulated (Figure S13) and removed from the data. Solid red lines are spectral simulations using the parameters listed in Table 2. The solid gray line is a spectral simulation of a diamagnetic impurity representing 5% of the total iron.

The Mössbauer spectra of **2**, shown in Figure 6, have been fit using the S = 1 spin Hamiltonian

$$H = D\left(\hat{S}_z^2 - \frac{2}{3}\right) + E(\hat{S}_x^2 - \hat{S}_y^2) + 2\beta\mathbf{B}\cdot\mathbf{S} + \mathbf{S}\cdot\mathbf{A}\cdot\mathbf{I} + g_n\beta_n\mathbf{B}\cdot\mathbf{I} + H_Q \quad (1a)$$

where

$$H_Q = \frac{eQV_{zz}}{12}\left[3\hat{I}_z^2 - \frac{15}{4} + \eta(\hat{I}_x^2 - \hat{I}_y^2)\right] \quad (1b)$$

D and E are the axial and rhombic zero-field-splitting (ZFS) parameters, respectively, and **A** is the magnetic hyperfine coupling tensor. The quadrupole interactions (H_Q) depend on the principal components of the electric field gradient (EFG) tensor **V** and are described by V_{zz} and the asymmetric parameter $\eta = (V_{xx} - V_{yy})/V_{zz}$. For all simulations, we assumed that the ZFS, EFG, and **A** tensors are collinear. In addition, E/D is fixed at zero and g values are assumed to be isotropic (g = 2.0). From the variable-field measurements, we determine that **2** has a large and positive D value (26 cm^{-1}) that arises from spin−orbit coupling of the S = 1 ground state with S = 2, 1, and 0 excited states. The D value of **2** is within experimental error the same as that for **3**, indicating that the S = 2 excited states of the two complexes are at comparable energies. This congruence of D values has important consequences for understanding the hydrogen-atom-transfer (HAT) reactivity of these two complexes (see Reactivity section below).

In addition to the major S = 1 oxoiron(IV) species, **2** contains 20% mononuclear high-spin iron(III) species (Figure S13) and an additional diamagnetic species representing 5% of the total iron (the gray solid curve above the top spectrum in Figure 6). The latter has an isomer shift δ of 0.44 mm s^{-1} and a quadrupole splitting ΔE_Q of 1.13 mm s^{-1} and likely corresponds to a minor diferric decay product.

The X-ray absorption near-edge structure region of the Fe K-edge XAS spectrum of **2** exhibits features at 7114.01 eV (preedge) and 7118.34 eV (rising edge) and a K-edge energy of 7124.54 eV. The first of these features derives from 1s → 3d transitions at the iron center, which increase in probability as the degree of 4p and 3d orbital mixing increases, and the second at approximately 7118 eV most likely arises from edge transitions (e.g., 1s → 4p). The energies of the aforementioned preedge and K-edge are effectively identical with those of the corresponding features in **3**,[52] which indicates that any differences between the electronic environments of these two complexes are not sufficient to impact the energy of these transitions. The preedge feature was found to have an area of 33 units, after scaling according to the amount of oxoiron(IV) present in the sample (it is assumed other components do not contribute significantly to the preedge area), which is identical with that reported for **3**.

The k^3-weighted EXAFS and Fourier-transformed data of **2** are displayed in Figure 7, and the results of EXAFS analysis (Table S2) are listed in Table 2. The Fourier-transformed data exhibit at least two main features at r' ∼ 1.5 and 2.5 Å. The peak at r' ∼ 1.5 Å is best fit with four Fe−N/O scatterers at 2.04 Å, which can be attributed to the nitrogen donors of the Me_2EBC ligand, plus a short Fe−O scatterer at 1.64 Å, a distance that is characteristic of the Fe^{IV}=O bond. The r' ∼ 2.5 Å feature can be fit by six Fe−C scatterers at a distance of 2.94 Å, which is typically seen for macrocyclic polyamine ligands and corresponds to the carbon framework of the Me_2EBC ligand. These values are broadly similar to those found for **3**,[52] with the main distinction being that the average Fe−N distance in **2** is

DOI: 10.1021/acs.inorgchem.5b00861
Inorg. Chem. 2015, 54, 7828−7839

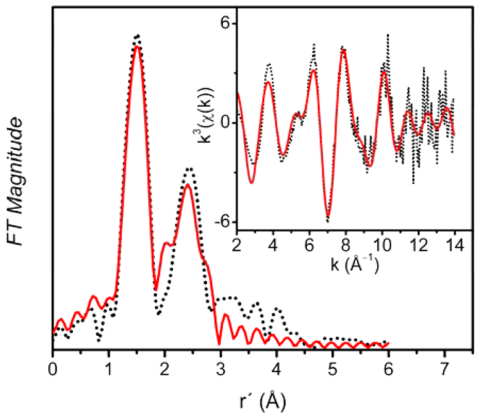

Figure 7. Fourier-transformed Fe K-edge EXAFS data (dotted black line) and corresponding best fit (solid red line) for **2**. The inset shows unfiltered EXAFS data $k^3[\chi(k)]$.

0.04 Å shorter, presumably because of the smaller/tighter binding cavity provided by Me_2EBC relative to TMC. The distances found experimentally are in reasonable agreement with values predicted by DFT calculations (Table 2).

DFT calculations at the B3LYP/6-311G level of theory were carried out for **2** (Table S3), and relevant comparisons with experimental data are presented in Table 2. The calculated Fe═O distance is in excellent agreement with the EXAFS-derived value, while the calculated average Fe−N distance is 0.04 Å longer than the value obtained from EXAFS. An overestimation of the Fe−N bond lengths of this magnitude is typically seen when using the B3LYP functional and was observed as well in the case of **3**.[52] The reliability of these optimized geometries was supported by good agreement between the calculated Mössbauer parameters and the corresponding experimental values. Space-filling models for the two geometry-optimized structures are compared in Figure 8. Initial inspection of these models suggested that the Fe^{IV}═O

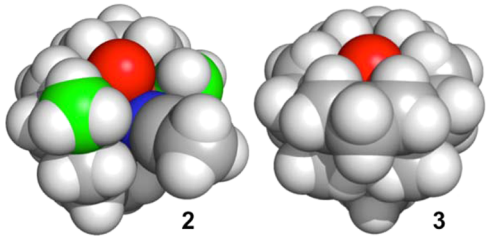

Figure 8. van der Waals radii space-filling models derived from geometry-optimized structures of **2** (left) and **3** (right). Atom color scheme: C, gray; H, white; N, blue; methyl C of the Me_2EBC supporting ligand for emphasis, green.

unit of **2** is not as shielded as that of **3** by the tetraazamacrocyclic ligand framework. This impression was validated by a comparison of the distances between the oxo ligand and the hydrogen atoms forming the oxo cavity (H_{cavity}), along with the corresponding Fe^{IV}═O···H_{cavity} angles in **2** and **3**. In the former complex, the O···H_{cavity} distances range between 2.40 and 2.80 Å with an average value of 2.61 Å, whereas they vary between 2.25 and 2.51 Å with an average value of 2.38 Å in the latter (Figure S14). Additionally, the smaller average Fe^{IV}═O···H_{cavity} angle of 91.3° (ranging between 84.0 and 98.3°) in **2** compared to 98.6° (ranging between 99.3 and 101.1°) in **3** is consistent with the oxo ligand being further out of the oxo pocket (Figure S15). Thus, the hydrogen atoms (H_{cavity}) in **3** are closer to the oxo moiety and may shield it further from incoming substrates. Also, the coordination of CH_3CN cis to the Fe^{IV}═O unit in **2** provides a "gap" (with an H_{Me}−O−H_{Me} angle of 111°) in the steric barrier surrounding the oxo ligand (the hydrogen atoms on CH_3CN are at least 4.74 Å away with an Fe^{IV}═O···H angle of 88.8°; Figure S16). The aforementioned differences in substrate access to the Fe^{IV}═O unit may be a factor in modulating its reactivity.

Reactivity of 2 (vs 3). The intermolecular oxygen-atom-transfer (OAT) and HAT reactivities of **2** were probed with various substrates and found to exhibit second-order kinetics in all cases. The observed rate constants (k_2) are listed in Table 3.

Table 3. Oxidation Rate Constants (k_2, M^{-1} s^{-1}) for $[Fe^{IV}(O)(L)]^{2+}$ Complexes 2 and 3[a]

	T (°C)	L = Me_2EBC (**2**)	L = TMC (**3**)
xanthene	0	12.8	0.39
DHA	0 25	7.4	0.14
		27 (KIE = 25)	0.5 (KIE = 10)[b]
CHD	0	7.4	0.12
fluorene	0	0.09	9.2×10^{-4}
PPh_3	−40	9.0	4.2×10^{-2}
	0	−[c]	5.9
PhSMe	0	0.41	9×10^{-4} [d]
E_{red} vs $Fc^{+/0}$ [e]	25	0.08	0.02

[a]For product yields, see Table S5. [b]Data from ref 16. [c]Too fast to determine by conventional kinetics. [d]We were not able to reproduce the k_2 values reported for the reaction of **3** with PhSMe in ref 60, which were about 1 order of magnitude higher (Figure S17 and Table S4). [e]Obtained by Fukuzumi's method[61] (Figure S18).

Complex **2** oxidized PPh_3 and PhSMe to corresponding oxides at rates consistent with the relative oxidizabilities of the two substrates. HAT reactions of **2** with substrates like xanthene, DHA, CHD, and fluorine were also studied. As found for other oxoiron(IV) complexes, a linear correlation was obtained when log k_2' values of HAT reactions ($k_2' = k_2$ divided by the number of equivalent C−H bonds on the substrate) were plotted versus the strength of the substrate C−H bonds being cleaved, indicating that the rate-determining step involves C−H bond cleavage (Figure 9). Interestingly, a large nonclassical H/D KIE of 25 was measured for the oxidation of dihydroanthracene by **2** at 25 °C.

When the rate constants associated with the oxidation of substrates by **2** are compared with the corresponding values for

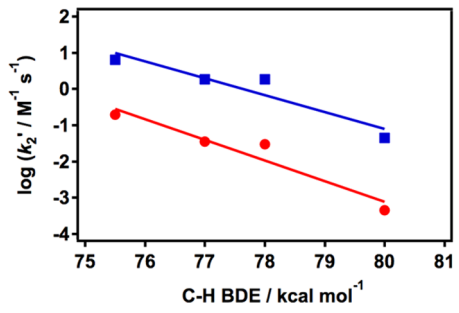

Figure 9. Plots of log k_2' values obtained at 0 °C versus the bond dissociation energies of substrate C−H bonds oxidized by **2** (blue squares) and **3** (red circles). Solid lines (red and blue) represent the best fits to the data.

DOI: 10.1021/acs.inorgchem.5b00861
Inorg. Chem. 2015, 54, 7828−7839

3 in Table 3, it is evident that 2 is more reactive than 3 in both HAT (30−100-fold) and OAT (200−600-fold) reactions. There is also a large difference between the H/D KIE values for the oxidation of DHA, 25 for 2 versus 10 for 3.[16] These reactivity differences are quite intriguing, given the fact that the macrocyclic ligands of 2 and 3 provide essentially identical donors but adopt different topologies. (Although it is not strictly the case, 2 and 3 may be construed as approximate geometrical isomers of each other.) Furthermore, the fact that the D values determined for 2 and 3 are the same within experimental error suggests that their electronic structures are comparable. Thus, the typical argument used in the two-state-reactivity (TSR) model of related complexes having different S = 2 excited-state energy levels[62] cannot be applied to the 2/3 pair.

A role for ligand topology in modulating the reactivity has been demonstrated for two pairs of isomers among the oxoiron(IV) complexes characterized to date. These are the only two examples for which the reactivity data has been reported (Figure 10). One pair consists of the cis-α and cis-β

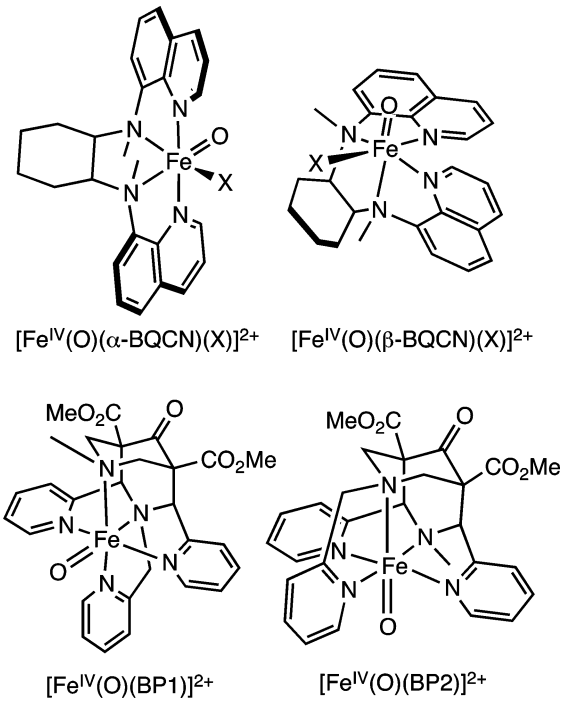

Figure 10. Two pairs of oxoiron(IV) complexes that differ with respect to the ligand topology.

isomers of $[Fe^{IV}(O)(BQCN)]^{2+}$ described by Nam et al., where the quinoline rings are oriented respectively trans and cis to each other.[63] The cis-α isomer is more reactive than the cis-β isomer by 10−20-fold with respect to HAT and 100-fold with respect to OAT. The other pair consists of the $[Fe^{IV}(O)(BP1)]^{2+}$ and $[Fe^{IV}(O)(BP2)]^{2+}$ complexes of Comba et al.,[64] which differ in the orientations of two pyridine rings relative to the Fe=O bond; the BP2 isomer with two pyridine rings perpendicular to the Fe=O bond is more reactive by 20−40-fold with respect to HAT and 100-fold with respect to OAT.[59] Thus, the effects of a change in the ligand topology are comparable for the BQCN and BP pairs of complexes.

The reactivity difference within each pair of complexes can be qualitatively rationalized by differences in the $Fe^{IV/III}$ reduction potentials between the two members of each pair, 0.11 V for the BQCN pair[63] and 0.25 V for the BP pair.[59] In both cases, the isomer with the more positive reduction potential is the more reactive complex. These pairwise trends are in line with that found for a series of five $[Fe^{IV}(O)(N5)]$ complexes, where N5 is a pentadentate ligand with a combination of pyridine and tertiary amine donors.[59] $[Fe^{IV}(O)(BP1)]$ and $[Fe^{IV}(O)(BP2)]$ are in fact members of this series. Observed for the series is a linear correlation for the logarithms of the second-order OAT rate constants for PhSMe versus their $Fe^{IV/III}$ reduction potentials, and the HAT values exhibit correlations with similar slopes. However, the even smaller difference (0.06 V) between the $Fe^{IV/III}$ potentials of found for 2 and 3 (Table 3) makes it difficult to apply the reduction potential argument to rationalize the observed reactivity differences. Clearly, other factors besides the redox potential must modulate the reactivity.

Another obvious factor to consider is the accessibility of the Fe=O unit for reaction with substrates. On the basis of DFT calculations of 2 and 3 (vide supra, Figure 8), the Fe=O unit of 2 appears to be more accessible than that of 3. The oxo ligand of 3 is well shielded by the hydrogen atoms of the TMC macrocycle, particularly for a substrate attack trajectory perpendicular to the Fe=O bond that is required for interaction with the singly occupied π^* orbitals of the S = 1 Fe=O unit.[16,38] On the other hand, the more open topology of the Me_2EBC macrocycle should allow easier access to the Fe=O unit via this trajectory. This possibility of a π^* attack trajectory was tested by comparing the oxidation rates of DHA and CHD, substrates with comparable C−H bond strength but different steric bulk. However, as can be seen in Table 3, the rates of DHA and CHD oxidation for 2 are not much different from each other, and the corresponding rates for 3 are also similar to each other but much slower than those for 2. From these comparisons, we surmise that there is no significant steric barrier for the HAT reactions of these two complexes. It is likely then that the HAT reactions of 2 and 3 do not occur via the π^* trajectory but instead take place by the much less hindered σ^* trajectory, which is available only on the S = 2 excited-state surface.[38,51,65,66] In support of the generality of this σ^* mechanism for HAT, we note that comparable DHA and CHD oxidation rates have, in fact, been observed for a number of S = 1 oxoiron(IV) complexes.[67] Comba and co-workers also reached a similar conclusion in their efforts to understand the relative HAT reactivity of the BP isomers discussed earlier. Their DFT and force-field calculations carried out on this pair of complexes afford computed barriers for the rate-determining hydrogen-atom-abstraction step on the S = 2 excited-state surface via the σ^* trajectory that differ by 0.6 kcal mol^{-1}, in accordance with the experimental data.[64,68]

Additional DFT calculations were thus carried out to investigate the reactivity differences between 2 and 3 with respect to DHA oxidation via HAT. The UB3LYP/B1-optimized geometries for 2 and 3 together with relevant iron−ligand distances in angstroms are presented in Figure S19. The main conclusions derived from these calculations are presented here in the main text; all of the corresponding reactivity data are reported in Table S6. Both reactions exhibit a typical TSR scenario,[62,65,66,69] in which the S = 2 transition state, ^{5}TS, lies well below that of the S = 1 species, ^{3}TS. At all of the levels of theory employed, 2 was found to be more reactive than 3 (Table S6), in line with experimental observations. Table 4 shows the free-energy barriers at the highest level

DOI: 10.1021/acs.inorgchem.5b00861
Inorg. Chem. 2015, 54, 7828−7839

Table 4. Calculated Imaginary Frequencies in the TSs, Free-Energy Barriers, and KIEs for the $S = 1$ Process and for a TSR Scenario via the $S = 2$ TS

					KIE		
oxidant	species	ν_{im} (cm^{-1})	$\Delta G^{\ddagger}_{273\ K}$ [a]	$\Delta G^{\ddagger}_{exp}$ [a]	$S = 1$	$S = 1 \rightarrow S = 2$	KIE_{exp}
2	^{3}TS	*i*1986	32.2		284	20	25
	^{5}TS	*i*1464	17.5[b]	14.8		20	25
3	^{3}TS	*i*2088	34.1		54	15	10
	^{5}TS	*i*1346	20.3[b]	17.0		15	10

[a] In kilocalories per mole using B3 for the computational values and the Eyring equation for the experimental values. [b] These are tunneling-corrected barriers (the correction is 1.3 kcal mol^{-1} for **2** and **3**). The barrier datum for **3** in ref 65 was obtained with a different solvent correction protocol than that in the present study (using PCM in *Gaussian09*). Note that the higher reactivity of **2** versus **3** is reproduced here at all of the computational levels.

($\Delta G^{\ddagger}$), imaginary frequencies of the TSs (ν_{im}), and the corresponding KIE values calculated for the reactions commencing on the $S = 1$ reactant state and passing via ^{5}TS, along with experimental values. It is seen that the calculations reproduce the trends in the free-energy barriers for the TSR scenario, although the absolute values of the barriers after tunneling corrections are a bit larger than the experimental values by about 3 kcal mol^{-1}. The calculations also reproduce the observation that both HAT processes involve significant tunneling, which is larger for **2**. The computed KIE values are accordingly 20 for **2** and 15 for **3**, in reasonable agreement with the experimentally observed KIEs of 25 and 10, respectively. Table 4 further lists the calculated KIEs for the two reactions proceeding on the $S = 1$ surface. *These huge KIEs are clearly much larger than the ones involving passage on the S = 2 surface*, thus supporting the previous predictions that KIE can serve as a probe of the reacting spin state.[65]

As clearly illustrated in Figure 11, ^{5}TS(**2**) has the scissile hydrogen atom equidistant from the carbon and oxygen atoms ($r_{CH} \sim r_{OH}$), and the C−H bond is slightly more elongated than that in ^{5}TS(**3**). This may account for the finding that the imaginary frequency of ^{5}TS(**2**) is a little bit higher (~120 cm^{-1}) than that of ^{5}TS(**3**), thereby leading to a higher KIE.

What then is the factor that lowers the HAT barrier for **2** relative to **3**? To answer this question, one can generally express the barrier as a sum of the following two terms:[70−74]

$$\Delta E^{\ddagger} = \Delta E^{\ddagger}_{dist} + \Delta E^{\ddagger}_{int}$$

$\Delta E^{\ddagger}_{dist}$ is the distortion energy of the two reactants in their ^{5}TS geometries relative to their relaxed geometries at the $S = 1$ reactant state. $\Delta E^{\ddagger}_{int}$ is the interaction energy of the two fragments in ^{5}TS. $\Delta E^{\ddagger}_{dist}$ and $\Delta E^{\ddagger}_{int}$ were calculated using the following equations:

$$\Delta E^{\ddagger}_{dist} = E^{\ddagger}(S) + E^{\ddagger}(^5O) - [E(S) + E(^3O)] \quad (2a)$$

$$\Delta E^{\ddagger}_{int} = E(^5TS) - [E^{\ddagger}(S) + E^{\ddagger}(^5O)] \quad (2b)$$

where $E^{\ddagger}(S)$ and $E^{\ddagger}(^5O)$ are single-point energies of the separated substrate and quintet-state oxidant fragments in the TS. Because the reactants start at the $S = 1$ ground state and cross over to the $S = 2$ surface during TSR, we must first ascertain that the initial $S = 1/S = 2$ energy gap does not affect the relative distortion energies. Indeed, these energy gaps are

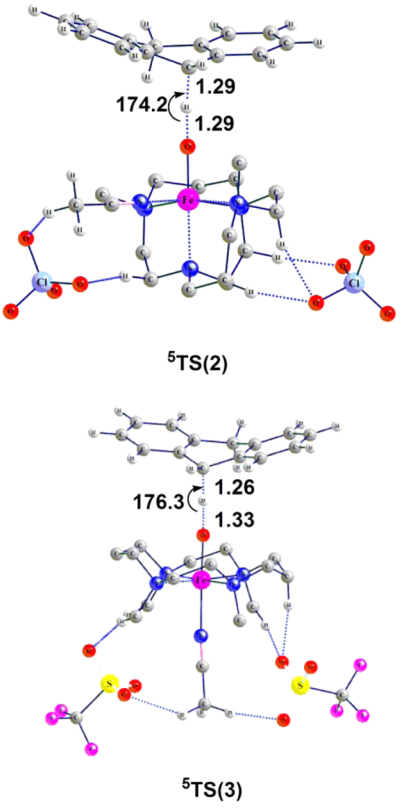

Figure 11. UB3LYP/B1-optimized geometries with important geometrical parameters (distances in angstroms and angles in degrees) for the TSs. Only selected hydrogen atoms are shown for clarity.

identical for **2** and **3** (see Table S8), as also deduced experimentally from their essentially identical D values (see Table 1).

Having ascertained that the $S = 1/S = 2$ energy gap does not contribute to the terms in eqs 2a and 2b, we can inspect the distortion and interaction energies in Table 5 (see the details in

Table 5. Distortion and Interaction Energies (kcal mol^{-1}) Calculated at the B3 Level of Theory

reaction	$\Delta E^{\ddagger}_{dist}$	$\Delta E^{\ddagger}_{int}$
2 + DHA	21.4	−7.3
3 + DHA	18.1	−2.4

Tables S10, parts 1 and 2, and S11 presented in the Supporting Information). It is seen that the reaction of **2** with DHA possesses a higher distortion energy ($\Delta E^{\ddagger}_{dist}$ = 21.4 kcal mol^{-1}) than the corresponding reaction of **3** ($\Delta E^{\ddagger}_{dist}$ = 18.1 kcal mol^{-1}). This energy difference of 3.3 kcal mol^{-1} is mainly due to the higher distortion of the DHA substrate (2.5 kcal mol^{-1}) in the ^{5}TS for **2**. However, Table 5 also shows that the interaction energy $\Delta E^{\ddagger}_{int}$ is significantly more favorable in ^{5}TS(**2**+DHA) than in ^{5}TS(**3**+DHA), indicating that ^{5}TS(**2**+DHA) is stabilized relatively more by electrostatic interaction and orbital mixing than ^{5}TS(**3**+DHA) and suffers less Pauli repulsion. Our calculations show that the electrostatic interaction contributes only ca. 1 kcal mol^{-1}, and the Pauli repulsions are also slightly less for ^{5}TS(**2**+DHA) (see the average distances in Figure S20. Hence, TS stabilization is dominated mainly by orbital mixing. Orbital mixing is, in turn, controlled by the ability of the oxidant to make an O---H bond

DOI: 10.1021/acs.inorgchem.5b00861
Inorg. Chem. 2015, 54, 7828−7839

in the corresponding TS. This capability of the oxidant can be predicted from the spin density on the oxygen atom of the Fe=O oxidant.[75] Even at the stage of the relaxed quintet-state oxidants, the spin-density values on the oxygen atoms of **2** and **3** are different, i.e., 0.74 and 0.64, respectively. En route to ^{5}TS, the difference between these values grows, becoming 0.71 and 0.54 for **2** and **3**, respectively (see also Tables S12 and S13). So, we can safely argue that the oxyl character ($O^\bullet$) of the Fe=O moiety of **2** is significantly larger than that of **3**. Consequently, the O---H bond in the TS is stronger for **2** than for **3**, and this is the main reason why ^{5}TS(**2**+DHA) is stabilized relative to its fragments. It follows therefore that the reactants **2** and DHA pay slightly more in terms of distortion energies in order to gain a more favorable bond-making interaction in the TS. So, considering all of the aforementioned factors, we can understand why **2** is more reactive than **3**.

CONCLUSIONS

Herein, we have detailed the synthesis, spectroscopic properties, and reactivity of the oxoiron(IV) complex **2** and compared it with the extensively studied complex **3**. Both Me_2EBC and TMC are tetradentate *N*-tetraalkylcyclam ligands that possess essentially identical donor atoms. Whereas the former enforces a geometry that allows the coordination of two additional cis ligands, the latter forms complexes with these sites disposed trans to one another. As a consequence, **2** and **3** represent a unique opportunity to compare two systems possessing effectively identical coordination spheres, differing only in the position of the solvent-labile site cis/trans to Fe^{IV}=O, in terms of their spectroscopic and reactivity properties. Indeed, the differing coordination geometries of **2** and **3** result in distinct UV−vis, Raman, and Mössbauer features. However, both complexes have comparable $Fe^{IV/III}$ potentials and exhibit essentially identical ZFS values, which implies that their respective S = 2 excited states are at comparable energies. Despite these similarities, **2** is 30−600-fold more reactive than **3** with respect to HAT and OAT reactions. DFT calculations reproduce the higher HAT reactivity of **2**, which is attributed to the greater oxyl character acquired by the oxo atom of the ^{5}**2** fragment in ^{5}TS. The reactivity data presented herein comparing **2** and **3**, together with the recent results of Mandal et al.[65] and Nam et al. on Fe(13-TMC) complexes,[60,76] serve to emphasize what a gold mine of information is provided by even the subset of oxoiron(IV) complexes supported by cyclam ligands and demonstrate that our understanding of the reactivity of nonheme oxoiron(IV) complexes remains incomplete and justifies continued investigation.

ASSOCIATED CONTENT

Supporting Information

The Supporting Information is available free of charge on the ACS Publications website at DOI: 10.1021/acs.inorgchem.5b00861.

Kinetic data, ESI-MS data, additional XAS data and analysis, additional Mössbauer data, variable-temperature ^{1}H NMR spectra of **1**, Mulliken spin densities and charges, and Cartesian coordinates of the geometry-optimized structures of **2** and **3** (PDF)

X-ray crystallographic data (CIF)

AUTHOR INFORMATION

Corresponding Authors

*E-mail: ysguo@andrew.cmu.edu.
*E-mail: emunck@cmu.edu.
*E-mail: sason@yfaat.ch.huji.ac.il.
*E-mail: larryque@umn.edu.

Present Addresses

$^\perp$J.E.: Division of Chemistry and Biological Chemistry, School of Physical and Mathematical Sciences, Nanyang Technological University, 21 Nanyang Link, Singapore 637371, Singapore.
$^\parallel$M.A.C.: Colorado State University - Pueblo, Pueblo, CO 81001.

Notes

The authors declare no competing financial interest.

ACKNOWLEDGMENTS

This work was supported by grants from the U.S. National Science Foundation (Grants CHE-1058248 and CHE-1361773 to L.Q. and Grant CHE-1305111 to E.M.) and a postdoctoral fellowship from the National Institutes of Health (NIH; ES017390 to M.A.C.). S.S. acknowledges support from the Israel Science Foundation (Grant 1183/13). XAS data were collected on beamline 7-3 at the SSRL. Use of the SSRL of the SLAC National Accelerator Laboratory is supported by the U.S. Department of Energy, Office of Science, Office of Basic Energy Sciences, under Contract DE-AC02-76SF00515. The SSRL Structural Molecular Biology Program is supported by the DOE Office of Biological and Environmental Research and by the NIH, National Institute of General Medical Sciences (NIGMS; including P41GM103393). The contents of this publication are solely the responsibility of the authors and do not necessarily represent the official views of NIGMS or NIH. We thank Drs. Matthew Latimer, Allyson Aranda, and Erik Nelson for their excellent technical support of our XAS experiments. X-ray crystallographic data collection and structure solutions were conducted by Dr. Victor G. Young, Jr. at the X-ray Crystallographic Laboratory, Department of Chemistry, University of Minnesota.

REFERENCES

(1) Krebs, C.; Galonic Fujimori, D.; Walsh, C. T.; Bollinger, J. M., Jr. *Acc. Chem. Res.* **2007**, *40*, 484.
(2) Kovaleva, E. G.; Lipscomb, J. D. *Nat. Chem. Biol.* **2008**, *4*, 186.
(3) Price, J. C.; Barr, E. W.; Tirupati, B.; Bollinger, J. M., Jr.; Krebs, C. *Biochemistry* **2003**, *42*, 7497.
(4) Hoffart, L. M.; Barr, E. W.; Guyer, R. B.; Bollinger, J. M., Jr.; Krebs, C. *Proc. Natl. Acad. Sci. U. S. A.* **2006**, *103*, 14738.
(5) Eser, B. E.; Barr, E. W.; Frantom, P. A.; Saleh, L.; Bollinger, J. M., Jr.; Krebs, C.; Fitzpatrick, P. F. *J. Am. Chem. Soc.* **2007**, *129*, 11334.
(6) Galonic, D. P.; Barr, E. W.; Walsh, C. T.; Bollinger, J. M., Jr.; Krebs, C. *Nat. Chem. Biol.* **2007**, *3*, 113.
(7) Matthews, M. L.; Krest, C. M.; Barr, E. W.; Vaillancourt, F. H.; Walsh, C. T.; Green, M. T.; Krebs, C.; Bollinger, J. M., Jr. *Biochemistry* **2009**, *48*, 4331.
(8) Panay, A. J.; Lee, M.; Krebs, C.; Bollinger, J. M., Jr.; Fitzpatrick, P. F. *Biochemistry* **2011**, *50*, 1928.
(9) Sinnecker, S.; Svensen, N.; Barr, E. W.; Ye, S.; Bollinger, J. M.; Neese, F.; Krebs, C. *J. Am. Chem. Soc.* **2007**, *129*, 6168.
(10) Wong, S. D.; Srnec, M.; Matthews, M. L.; Liu, L. V.; Kwak, Y.; Park, K.; Bell Iii, C. B.; Alp, E. E.; Zhao, J.; Yoda, Y.; Kitao, S.; Seto, M.; Krebs, C.; Bollinger, J. M.; Solomon, E. I. *Nature* **2013**, *499*, 320.
(11) McDonald, A. R.; Que, L., Jr. *Coord. Chem. Rev.* **2013**, *257*, 414.
(12) Hohenberger, J.; Ray, K.; Meyer, K. *Nat. Commun.* **2012**, *3*, 720.

DOI: 10.1021/acs.inorgchem.5b00861
Inorg. Chem. 2015, 54, 7828−7839

(13) de Visser, S. P.; Rohde, J.-U.; Lee, Y.-M.; Cho, J.; Nam, W. *Coord. Chem. Rev.* **2013**, *257*, 381.
(14) Barefield, E. K. *Coord. Chem. Rev.* **2010**, *254*, 1607.
(15) Rohde, J.-U.; In, J.-H.; Lim, M. H.; Brennessel, W. W.; Bukowski, M. R.; Stubna, A.; Münck, E.; Nam, W.; Que, L., Jr. *Science* **2003**, *299*, 1037.
(16) Sastri, C. V.; Lee, J.; Oh, K.; Lee, Y. J.; Lee, J.; Jackson, T. A.; Ray, K.; Hirao, H.; Shin, W.; Halfen, J. A.; Kim, J.; Que, L., Jr.; Shaik, S.; Nam, W. *Proc. Natl. Acad. Sci. U. S. A.* **2007**, *104*, 19181.
(17) Thibon, A.; England, J.; Martinho, M.; Young, V. G.; Frisch, J. R.; Guillot, R.; Girerd, J.-J.; Münck, E.; Que, L., Jr.; Banse, F. *Angew. Chem., Int. Ed.* **2008**, *47*, 7064.
(18) England, J.; Bigelow, J. O.; Van Heuvelen, K. M.; Farquhar, E. R.; Martinho, M.; Meier, K. K.; Frisch, J. R.; Münck, E.; Que, L., Jr. *Chem. Sci.* **2014**, *5*, 1204.
(19) Yin, G.; McCormick, J. M.; Buchalova, M.; Danby, A. M.; Rodgers, K.; Day, V. W.; Smith, K.; Perkins, C. M.; Kitko, D.; Carter, J. D.; Scheper, W. M.; Busch, D. H. *Inorg. Chem.* **2006**, *45*, 8052.
(20) Xu, A.; Xiong, H.; Yin, G. *Chem. - Eur. J.* **2009**, *15*, 11478.
(21) Feng, Y.; England, J.; Que, L., Jr. *ACS Catal.* **2011**, *1*, 1035.
(22) Hubin, T. J.; McCormick, J. M.; Collinson, S. R.; Buchalova, M.; Perkins, C. M.; Alcock, N. W.; Kahol, P. K.; Raghunathan, A.; Busch, D. H. *J. Am. Chem. Soc.* **2000**, *122*, 2512.
(23) Macikenas, D.; Skrzypczak-Jankun, E.; Protasiewicz, J. D. *J. Am. Chem. Soc.* **1999**, *121*, 7164.
(24) Sheldrick, G. M. *CELL_NOW*; University of Gottingen: Gottingen, Germany, 2008.
(25) Sheldrick, G. M. *TWINABS*; University of Gottingen: Gottingen, Germany, 2008.
(26) *SAINT*, version 6.45; Bruker Analytical X-ray Systems: Madison, WI, 2003.
(27) *SHELXTL*, version 6.14; Bruker Analytical X-ray Systems: Madison, WI, 2000.
(28) George, G. N. *EXAFSPAK*; Stanford Synchrotron Radiation Laboratory, Stanford Linear Accelerator Center: Stanford, CA, 2000.
(29) Ankudinov, A. L.; Ravel, B.; Rehr, J. J.; Conradson, S. D. *Phys. Rev. B: Condens. Matter Mater. Phys.* **1998**, *58*, 7565.
(30) Ravel, B.; Newville, M. *J. Synchrotron Radiat.* **2005**, *12*, 537.
(31) Westre, T. E.; Kennepohl, P.; DeWitt, J. G.; Hedman, B.; Hodgson, K. O.; Solomon, E. I. *J. Am. Chem. Soc.* **1997**, *119*, 6297.
(32) Wojdyr, M. *J. Appl. Crystallogr.* **2010**, *43*, 1126.
(33) Frisch, M. J.; Schlegel, H. B.; Scuseria, G. E.; Robb, M. A.; Cheeseman, J. R.; Scalmani, G.; Barone, V.; Mennucci, B.; Petersson, G. A.; Nakatsuji, H.; Caricato, M.; Li, X.; Hratchian, H. P.; Izmaylov, A. F.; Bloino, J.; Zheng, G.; Sonnenberg, J. L.; Hada, M.; Ehara, M.; Toyota, K.; Fukuda, R.; Hasegawa, J.; Ishida, M.; Nakajima, T.; Honda, Y.; Kitao, O.; Nakai, H.; Vreven, T.; Montgomery, J. A., Jr.; Peralta, J. E.; Ogliaro, F.; Bearpark, M.; Heyd, J. J.; Brothers, E.; Kudin, K. N.; Staroverov, V. N.; Keith, T.; Kobayashi, R.; Normand, J.; Raghavachari, K.; Rendell, A.; Burant, J. C.; Iyengar, S. S.; Tomasi, J.; Cossi, M.; Rega, N.; Millam, J. M.; Klene, M.; Knox, J. E.; Cross, J. B.; Bakken, V.; Adamo, C.; Jaramillo, J.; Gomperts, R.; Stratmann, R. E.; Yazyev, O.; Austin, A. J.; Cammi, R.; Pomelli, C.; Ochterski, J. W.; Martin, R. L.; Morokuma, K.; Zakrzewski, V. G.; Voth, G. A.; Salvador, P.; Dannenberg, J. J.; Dapprich, S.; Daniels, A. D.; Farkas, O.; Foresman, J. B.; Ortiz, J. V.; Cioslowski, J.; Fox, D. J. *Gaussian09*; Gaussian, Inc.: Wallingford, CT, 2010.
(34) Vrajmasu, V.; Bominaar, E.; Meyer, J.; Münck, E. *Inorg. Chem.* **2002**, *41*, 6358.
(35) *Jaguar*, version 8.0; LLC: New York, 2011.
(36) Duncan, W. T.; Bell, R. L.; Truong, T. N. *J. Comput. Chem.* **1998**, *19*, 1039.
(37) McDonald, A. R.; Bukowski, M. R.; Farquhar, E. R.; Jackson, T. A.; Koehntop, K. D.; Seo, M. S.; De Hont, R. F.; Stubna, A.; Halfen, J. A.; Münck, E.; Nam, W.; Que, L., Jr. *J. Am. Chem. Soc.* **2010**, *132*, 17118.
(38) Wilson, S. A.; Chen, J.; Hong, S.; Lee, Y.-M.; Clemancey, M.; Garcia-Serres, R.; Nomura, T.; Ogura, T.; Latour, J.-M.; Hedman, B.; Hodgson, K. O.; Nam, W.; Solomon, E. I. *J. Am. Chem. Soc.* **2012**, *134*, 11791.
(39) Zang, Y.; Kim, J.; Dong, Y.; Wilkinson, E. C.; Appelman, E. H.; Que, L., Jr. *J. Am. Chem. Soc.* **1997**, *119*, 4197.
(40) Blakesley, D. W.; Payne, S. C.; Hagen, K. S. *Inorg. Chem.* **2000**, *39*, 1979.
(41) Sastri, C. V.; Park, M. J.; Ohta, T.; Jackson, T. A.; Stubna, A.; Seo, M. S.; Lee, J.; Kim, J.; Kitagawa, T.; Münck, E.; Que, L., Jr.; Nam, W. *J. Am. Chem. Soc.* **2005**, *127*, 12494.
(42) Company, A.; Gomez, L.; Fontrodona, X.; Ribas, X.; Costas, M. *Chem. - Eur. J.* **2008**, *14*, 5727.
(43) Spannring, P.; Prat, I.; Costas, M.; Lutz, M.; Bruijnincx, P. C. A.; Weckhuysen, B. M.; Klein Gebbink, R. J. M. *Catal. Sci. Technol.* **2014**, *4*, 708.
(44) Prat, I.; Company, A.; Corona, T.; Parella, T.; Ribas, X.; Costas, M. *Inorg. Chem.* **2013**, *52*, 9229.
(45) Gütlich, P.; Garcia, Y.; Goodwin, H. A. *Chem. Soc. Rev.* **2000**, *29*, 419.
(46) Gütlich, P. *Struct. Bonding (Berlin)* **1981**, *44*, 83.
(47) Bryliakov, K. P.; Duban, E. A.; Talsi, E. P. *Eur. J. Inorg. Chem.* **2005**, *2005*, 72.
(48) Britovsek, G. J. P.; England, J.; White, A. J. P. *Inorg. Chem.* **2005**, *44*, 8125.
(49) England, J.; Britovsek, G. J. P.; Rabadia, N.; White, A. J. P. *Inorg. Chem.* **2007**, *46*, 3752.
(50) Decker, A.; Rohde, J.-U.; Que, L., Jr.; Solomon, E. I. *J. Am. Chem. Soc.* **2004**, *126*, 5378.
(51) Decker, A.; Rohde, J.-U.; Klinker, E. J.; Wong, S. D.; Que, L., Jr.; Solomon, E. I. *J. Am. Chem. Soc.* **2007**, *129*, 15983.
(52) Jackson, T. A.; Rohde, J.-U.; Seo, M. S.; Sastri, C. V.; DeHont, R.; Stubna, A.; Ohta, T.; Kitagawa, T.; Münck, E.; Nam, W.; Que, L., Jr. *J. Am. Chem. Soc.* **2008**, *130*, 12394.
(53) Krzystek, J.; England, J.; Ray, K.; Ozarowski, A.; Smirnov, D.; Que, L., Jr.; Telser, J. *Inorg. Chem.* **2008**, *47*, 3483.
(54) Ray, K.; England, J.; Fiedler, A. T.; Martinho, M.; Münck, E.; Que, L., Jr. *Angew. Chem., Int. Ed.* **2008**, *47*, 8068.
(55) Klinker, E. J.; Kaizer, J.; Brennessel, W. W.; Woodrum, N. L.; Cramer, C. J.; Que, L., Jr. *Angew. Chem., Int. Ed.* **2005**, *44*, 3690.
(56) Zheng, H.; Yoo, S. J.; Münck, E.; Que, L., Jr. *J. Am. Chem. Soc.* **2000**, *122*, 3789.
(57) Codola, Z.; Costas, M.; Lloret-Fillol, J.; Gomez, L.; Kleespies, S. T.; Que, L., Jr. *Nat. Commun.* **2015**, *6*, 5865.
(58) Company, A.; Prat, I.; Frisch, J. R.; Mas-Balleste, R.; Güell, M.; Juhasz, G.; Ribas, X.; Münck, E.; Luis, J. M.; Que, L., Jr.; Costas, M. *Chem. - Eur. J.* **2011**, *17*, 1622.
(59) Wang, D.; Ray, K.; Collins, M. J.; Farquhar, E. R.; Frisch, J. R.; Gomez, L.; Jackson, T. A.; Kerscher, M.; Waleska, A.; Comba, P.; Costas, M.; Que, L., Jr. *Chem. Sci.* **2013**, *4*, 282.
(60) Hong, S.; So, H.; Yoon, H.; Cho, K.-B.; Lee, Y.-M.; Fukuzumi, S.; Nam, W. *Dalton Trans.* **2013**, *42*, 7842.
(61) Lee, Y.-M.; Kotani, H.; Suenobu, T.; Nam, W.; Fukuzumi, S. *J. Am. Chem. Soc.* **2008**, *130*, 434.
(62) Hirao, H.; Que, L., Jr.; Nam, W.; Shaik, S. *Chem. - Eur. J.* **2008**, *14*, 1740.
(63) Hong, S.; Lee, Y.-M.; Cho, K.-B.; Sundaravel, K.; Cho, J.; Kim, M. J.; Shin, W.; Nam, W. *J. Am. Chem. Soc.* **2011**, *133*, 11876.
(64) Anastasi, A. E.; Comba, P.; McGrady, J.; Lienke, A.; Rohwer, H. *Inorg. Chem.* **2007**, *46*, 6420.
(65) Mandal, D.; Ramanan, R.; Usharani, D.; Janardanan, D.; Wang, B.; Shaik, S. *J. Am. Chem. Soc.* **2015**, *137*, 722.
(66) Kumar, D.; Hirao, H.; Que, L., Jr.; Shaik, S. *J. Am. Chem. Soc.* **2005**, *127*, 8026.
(67) Kleespies, S. T.; Oloo, W. N.; Mukherjee, A.; Que, L., Jr. *Inorg. Chem.* **2015**, *54*, 5053.
(68) Barman, P.; Vardhaman, A. K.; Martin, B.; Woerner, S. J.; Sastri, C. V.; Comba, P. *Angew. Chem., Int. Ed.* **2015**, *54*, 2095.
(69) Schröder, D.; Shaik, S.; Schwarz, H. *Acc. Chem. Res.* **2000**, *33*, 139.
(70) Kitaura, K.; Morokuma, K. *Int. J. Quantum Chem.* **1976**, *10*, 325.

DOI: 10.1021/acs.inorgchem.5b00861
Inorg. Chem. 2015, 54, 7828−7839

(71) Ess, D. H.; Houk, K. N. *J. Am. Chem. Soc.* **2008**, *130*, 10187.
(72) Ziegler, T.; Rauk, A. *Inorg. Chem.* **1979**, *18*, 1558.
(73) Bickelhaupt, F. M.; Diefenbach, A.; de Visser, S. P.; de Koning, L. J.; Nibbering, N. M. M. *J. Phys. Chem. A* **1998**, *102*, 9549.
(74) Usharani, D.; Janardanan, D.; Li, C.; Shaik, S. *Acc. Chem. Res.* **2013**, *46*, 471.
(75) For an extensive review regarding the role of the oxyl, see: Dietl, N.; Schlangen, M.; Schwarz, H. *Angew. Chem., Int. Ed.* **2012**, *51*, 5544.
(76) Hong, S.; Wang, B.; Seo, M. S.; Lee, Y.-M.; Kim, M. J.; Kim, H. R.; Ogura, T.; Garcia-Serres, R.; Clemancey, M.; Latour, J.-M.; Nam, W. *Angew. Chem., Int. Ed.* **2014**, *53*, 6388.

DOI: 10.1021/acs.inorgchem.5b00861
Inorg. Chem. 2015, 54, 7828−7839